ORIGINAL ARTICLE

Perfluorooctyl bromide nanoemulsions holding MnO$_2$ nanoparticles with dual-modality imaging and glutathione depletion enhanced HIFU-eliciting tumor immunogenic cell death

Xinping Kuai[a,†], Yuefei Zhu[b,†], Zheng Yuan[c,†], Shengyu Wang[d,†], Lin Lin[a], Xiaodan Ye[e], Yiping Lu[a], Yu Luo[f], Zhiqing Pang[b,*], Daoying Geng[a,*], Bo Yin[a,*]

[a]Department of Radiology, Huashan Hospital, Fudan University, Shanghai 200040, China
[b]School of Pharmacy, Fudan University, Key Laboratory of Smart Drug Delivery, Ministry of Education, Shanghai 201203, China
[c]Department of Radiology, Shanghai First Maternity and Infant Hospital, Tongji University School of Medicine, Shanghai 201204, China
[d]Department of Radiology, Ruijin Hospital, Shanghai Jiao Tong University School of Medicine, Shanghai 201800, China
[e]Department of Radiology, Shanghai Chest Hospital, Shanghai Jiao Tong University, Shanghai 200030, China
[f]State Key Laboratory of High Performance Ceramics and Superfine Microstructure, School of Chemical Science and Engineering, Shanghai 200092, China

Abstract   Tumor-targeted immunotherapy is a remarkable breakthrough, offering the inimitable advantage of specific tumoricidal effects with reduced immune-associated cytotoxicity. However, existing platforms suffer from low efficacy, inability to induce strong immunogenic cell death (ICD), and restrained capacity of transforming immune-deserted tumors into immune-cultivated ones. Here, an innovative platform, perfluorooctyl bromide (PFOB) nanoemulsions holding MnO$_2$ nanoparticles (MBP), was developed to orchestrate cancer immunotherapy, serving as a theranostic nanoagent for MRI/CT dual-modality imaging and advanced ICD. By simultaneously depleting the GSH and eliciting the ICD effect *via* high-intensity focused ultrasound (HIFU) therapy, the MBP nanomedicine can regulate the tumor immune

microenvironment by inducing maturation of dendritic cells (DCs) and facilitating the activation of $CD8^+$ and $CD4^+$ T cells. The synergistic GSH depletion and HIFU ablation also amplify the inhibition of tumor growth and lung metastasis. Together, these findings inaugurate a new strategy of tumor-targeted immunotherapy, realizing a novel therapeutics paradigm with great clinical significance.

1. Introduction

Cancer immunotherapy, a validated and critically important approach for cancer treatment, have transformed treatment algorithms for numerous tumor types and achieved therapeutic advances in the past few years[1]. Despite the successful application of cancer immunotherapy across a wide range of human cancers, only a minority of patients with otherwise terminal cancer experienced life-altering durable survival from these therapies[2]. Such outcomes indicate the intricate biological process of the immunologic elimination of malignant cells[3]. In addition, the heterogeneity of cancers in different patients, the limited preclinical model, the complicate tumor immunosuppressive environment along with the chronic inflammatory states are making the cancer immunotherapy far away from being the cusp of "curing cancer"[4−6]. Although the induction of immunogenic cell death (ICD) may enable the release of key immunostimulatory or danger signals to effectively drive antitumor immunity, there are no clear guidelines for the clinical application of emerging ICD inducers. Besides, according to immune surveillance models, overtly malignant lesions only appear once neoplastic cells fully evade immune recognition and elimination, and this potentially fatal progression is closely associated with suppression of the various processes involved in damage-associated molecular patterns (DAMP) release and perception[7,8]. Indeed, advanced tumors usually display high antigenicity, but they effectively control immunogenicity through a variety of mechanisms operating on (or downstream of) adjuvanticity that greatly impair the efficiency of multiple chemo-, radio- and immunotherapeutic regimens[9].

High-intensity focused ultrasound (HIFU), a representative non-invasive therapeutic mode, can convert ultrasound energy to regional hyperthermia and induce cell death through the coagulation-necrosis route[10]. Of note, the energy released by HIFU is absorbed by the tissue, raising the temperature to 60−85 °C within a few seconds. The high temperature in the focus zone causes protein coagulation and cell membrane fusion, leading to tumor cell necrosis[11]. Further, by focusing the ultrasonic wave on the target position, the high-intensity irradiation will respond to the acoustic pressure wave to affect mechanical deformation and cavitation[10]. Although the nature of tumor antigens presented in the debris after HIFU ablation and the kinetics of their release into the circulation remain unclear, HIFU therapy of tumors is developing quickly. Theoretically, besides tumor ablation, HIFU treatment may promote the release of tumor antigens and bioactive molecules such as DAMP, thereby enhancing the antitumor immune responses[12,13]. In this context, modified HIFU regimens may not only focus on full ablation, but

also trigger ICD to simultaneously cope with primary tumors as well as distant metastasis.

Tumor cells have approximately fourfold higher levels of glutathione (GSH) than that in normal cells[14−16]. Indeed, the higher GSH levels in tumors can benefit cancer cells by enabling greater reactive oxygen species (ROS) detoxification, which is responsible for increasing resistance to chemo-, radio-, and photodynamic therapy[16−19]. In this regard, regulating of intracellular GSH metabolism is a potential approach, which may enhance robust ICD effect and efficient antitumor therapy. The combination of GSH-depletion with HIFU treatment will generate synergistic therapeutic efficacy and restore systemic antitumor immunity to efficiently eradicate malignant cells.

Previous studies have unveiled that manganese dioxide (MnO_2), which exhibits both Fenton-like Mn^{2+} delivery and superior GSH-depletion properties, can disrupt the cellular antioxidant defense system and enhance antitumor efficiency[14,20,21]. In addition, MnO_2 generate Mn^{2+} ions, which could be utilized as an agent for T1-weighted MR imaging[14,20,21]. Moreover, perfluorooctyl bromide (PFOB) is a desirable contrast medium for computed tomography imaging due to the presence of bromine[22,23]. The liquid PFOB might transform into microbubbles through a HIFU-induced vaporization process which could intensify the cavitation effect for enhancing the HIFU ablation[24−26].

Inspired by these two components, we inaugurated a novel multifunctional nanoemulsion platform, PFOB nanoemulsions holding MnO_2 nanoparticles (MBP) as a theranostic nanoagent for MRI/CT dual-modality imaging and advanced ICD immunotherapy (Fig. 1A). The MBP nanoemuslions could react with GSH to generate Mn^{2+} ions, which could enhance T1-weighted MR imaging. The PFOB might could cause robust mechanical stress enhancement during blasting and enhance tumor coagulative necrosis. Concomitantly, MnO_2 could deplete GSH, thus regulating the tumor microenvironment and enhancing HIFU-induced tumor ICD. Under the combination of MBP nanoemulsions and HIFU, tumor cells released DAMPs, such as surface-exposed calreticulin (CALR), adenosine triphosphate (ATP), and high mobility group protein B1 (HMGB1), which elicited maturation of dendritic cells (DCs) and subsequently facilitated activation of $CD8^+$ and $CD4^+$ T cells. The designed therapeutic regimen also achieved significant therapeutic effects in inhibiting both primary tumor growth and lung metastasis via a synergistic GSH depletion and HIFU-induced ICD (Fig. 1B). Hence, our study demonstrates and provides a tool and an immunotherapy strategy, which integrates diagnosis and treatment, to better tackle the cancer immunotherapy and realize the dual-modality imaging.
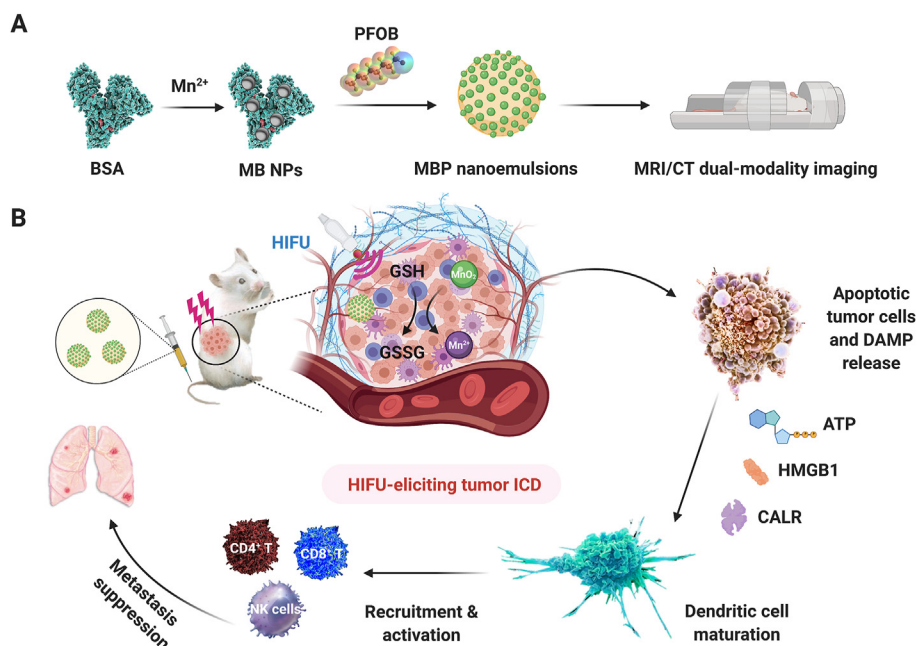
Figure 1 Schematic diagram of perfluorooctyl bromide nanoemulsions holding MnO_2 nanoparticles (MBP) with dual-modality imaging and GSH depletion enhancing HIFU-eliciting tumor immunogenic cell death. (A) Scheme of synthesis of MBP nanoemulsions with MRI/CT dual-modality imaging. (B) Scheme of action mechanism of MBP nanoemulsions to enhance HIFU-induced tumor immunogenic cell death. Dendritic cells: process antigen material and present it on the cell surface to the T cells of the immune system; effector cells: $CD8^+$ T cells, $CD4^+$ T cells, and NK cells may be activated and suppress the primary tumor and lung metastases.

2. Materials and methods

2.1. Chemicals and reagents

Bovine serum albumin (BSA), manganese chloride tetrahydrate ($MnCl_2 \cdot 4H_2O$), and sodium hydroxide (NaOH) were purchased from Aladdin, Shanghai, China. PFOB, glutathione (GSH), coumarin-6 (Cou-6), and Hoechst 33342 were obtained from Sigma−Aldrich, St. Louis, USA. GSH assay Kit, cell counting Kit-8 (CCK-8), 4′,6-diamidino-2-phenylindole (DAPI), DiD, and lysosomal staining lysotracker red were procured from KeyGen Biotech, Nanjing, China. Dulbecco's modified Eagle's medium (high glucose) (DMEM), trypsin, penicillin/streptomycin, and fetal bovine serum (FBS) were purchased from Gibco, CA, USA. Calreticulin rabbit monoclonal antibody, 2′,7′-dichlorodihydro-fluorescein diacetate (DCFH-DA), and ATP Assay Kit were purchased from Beyotime, Nantong, China. HMGB1 ELISA Kit was bought from Arigo Biolaboratories, Taiwan, China. Anti-SPARC Antibody was purchased from St. John's Laboratory, UK. TUNEL Assay Kit, anti-Calreticulin antibody, and anti-HMGB1 antibody were purchased from Abcam, Cambridge, UK. FITC anti-mouse CD11c antibody, PE anti-mouse CD86 antibody, APC anti-mouse CD80 antibody, FITC anti-mouse CD3 antibody, APC anti-mouse CD4 antibody, and PE anti-mouse CD8 antibody were purchased from BioLegend, CA, USA. All other reagents were of analytical grade and used without further purification.

2.2. Cells and animals

The 4T1 murine breast cancer and U87 MG human glioma cell lines were purchased from the Cell Bank of the Chinese Academy of Sciences (Shanghai, China). HUVEC cell line was bought from American Type Culture Collection (ATCC). All cell lines were cultured in DMEM medium with 10% FBS and 1% penicillin/streptomycin at 37 °C and 5% CO_2.

Female BALB/c mice and nude mice (4 weeks, 17−18 g) were purchased from Shanghai SLAC Laboratory Animal Co., Ltd. and housed under specific-pathogen free (SPF) conditions. All animal handling protocols were approved by the Animal Ethics Committee of Fudan University. To construct xenograft 4T1 tumor-bearing mice and establish the lung metastatic model[27], 4T1 cells (1×10^6) were suspended in PBS (100 μL) and inoculated subcutaneously into the right buttocks of female BALB/c mice. Three days after mice inoculated with 4T1 cells subcutaneously, the lung metastatic models were induced by an intravenous injection of 4T1 cells (2×10^5) into the tail vein.

2.3. Synthesis of MnO_2 nanoparticles and MBP nanoemulsions

MnO_2 nanoparticles (MB) were synthesized using the biomineralization reaction[28]. Briefly, 0.8 mL of $MnCl_2$ solution (100 mmol/L) was added into 12 mL of BSA solution (10 mg/mL) dropwise under magnetic stirring. After stirring for 5 min, the pH value of the mixed solution of $MnCl_2$ and BSA was adjusted to 11 with 1 mol/L NaOH. Then the reaction mixture solution was stirred at room temperature for 2 h to generate MB nanoparticles. The obtained MB nanoparticles were dialyzed for 2 days with deionized water to remove unreacted precursors. After the freeze-drying process, brown powders of MB nanoparticles were obtained.

MBP nanoemulsions were synthesized using sonic emulsification[25,29]. Briefly, 20 mg of MB nanoparticles were dissolved in 1 mL of ddH_2O. Two milliliters of MB with a concentration of 20 mg/mL and 60 μL of PFOB were added into a reaction tube with a total capacity of 10 mL. The reaction tube was cooled in an ice bath and the mixed solution was sonicated (2 s cooling, 2 s burst at 180 W) for 5 min by an ultrasonic processor (Xin Yi

ultrasonic equipment Co., Ltd., Ningbo, China). After sonication, MBP nanoemulsions were obtained.

Cou-6-labeled or DiD-labeled MBP nanoemulsions were prepared using the same steps except that Cou-6 or DiD was added to the MB before emulsification, and the nanoparticles were centrifuged in an ultrafiltration tube with a 30-kDa molecular weight cut-off at 4000 rpm for 30 min (Thermo Biofuge Stratos, Waltham, MA, USA) to remove the free cou-6 or DiD.

2.4. Characterization of MB and MBP

The morphology of MBP was investigated using Transmission Electron Microscopy (TEM, FEI Co., USA). The hydrodynamic diameters and zeta potential of nanoemulsions were measured by dynamic light scattering (DLS, Zetasizer Nano ZS, Malvern, UK). The concentration of manganese (Mn) in MB was measured by inductively coupled plasma optical emission spectrometer (ICP-OES, PerkinElmer, USA). The loading capacity of PFOB in MBP nanoemulsions was estimated by the ^{19}FNMR method as previously described[30,31]. The valence states of Mn in the MB were characterized via X-ray photoelectron spectroscopy (XPS, Thermo Scientific K-Alpha+, USA). The stability of the MBP in vitro was evaluated by monitoring the hydrodynamic size for 48 h at 4 °C in PBS and the absorbance value (OD) of 580 nm for 12 h at 37 °C in FBS by using a microplate reader.

2.5. In vitro CT and MRI of MBP

MBP nanoemulsions were diluted to different Mn concentrations (1, 0.5, 0.25, 0.125, 0.0625 and 0 mmol/L) in PBS with various pH values (7.4, 6.5 and 5.5) and different GSH concentrations (0, 5, and 10 mmol/L). Then, 1 mL of each solution was collected, and T_1-weighted MRI (T_1 mapping) was performed on a 3.0 T clinical scanner. Then, the T_1 relaxation rates (r_1) were calculated by T_1 values at different Mn concentrations.

In vitro CT imaging evaluations of MBP nanoemulsions at different PFOB concentrations were conducted on Aquilion™ Prime 128 CT at 25 °C. The following parameters were used: 120 kV for tube voltage, 70 mAs for current, 2 mm for slice spacing and slice thickness.

2.6. In vitro cellular uptake of MBP

The cellular uptake of MBP was studied using a confocal laser scanning microscopy (CLSM) and a flow cytometry. U87 or 4T1 cells were cultured in confocal dishes at a cell density of 1×10^4 cells/dish and allowed to attach for 24 h. After 24 h, the confocal dishes were washed with PBS. Then, the cells were incubated with cou-6-labeled MBP in DMEM medium at 4 μg/mL of Mn for 0, 1, 2, 4, and 6 h and stained with DAPI according to the manufacturer's instruction. The cells were imaged on a CLSM (Carl Zeiss, Germany).

For quantitative analysis, U87 or 4T1 cells (5×10^5 cells/well) were seeded in 6-well plates for 24 h and treated as previously described except that the cells were not stained with DAPI. Subsequently, U87 or 4T1 cells were harvested and resuspended in 0.3 mL of PBS. The fluorescence intensity of cells was detected by a flow cytometry (BD, USA).

2.7. In vitro co-localization of MBP with lysosomes

For in vitro co-localization of MBP nanoemulsions with lysosomes, U87 or 4T1 cells (8000 cells/well) were seeded in confocal dishes for 24 h. After 24 h, the confocal dishes were washed with PBS. Then, the cells were incubated with cou-6-labeled MBP in DMEM medium at 4 μg/mL of Mn for 0, 0.5, 1, 2 and 4 h, and stained with lysotracker red and Hoechst 33342 according to the manufacturer's protocols. The cells were imaged on a CLSM (Carl Zeiss, Germany).

2.8. In vitro cell viability test

Cell viability was evaluated by the CCK-8 method. The HUVEC, U87, and 4T1 cells (5×10^3 cells/well) were seeded in 96-well plates for 24 h and then exposed to MBP with different Mn concentrations ranging from 0 to 100 μg/mL for 24 or 48 h. After treatment, 10 μL of CCK-8 solution was added to each well containing 100 μL of DMEM and incubated for 1.5 h. Then, the OD was recorded at 450 nm. All experiments were repeated in triplicate.

The 4T1 cells were cultured and harvested as single-cell suspensions. Single-cell suspensions were irradiated by HIFU at 8.5 W for 0, 30, 60, 120 and 170 s, respectively, and the suspension temperature was monitored with a near-infrared thermal imaging camera thermographic system (Infra Tec, VarioCAM®hr research, German). After treatment, 4T1 cells (5×10^3 cells/well) were seeded in 96-well plates for 24 h and 10 μL of CCK-8 solution was added to each well containing 100 μL of DMEM and incubated for 1.5 h. Then, the OD was recorded at 450 nm. All experiments were repeated in triplicate.

2.9. In vitro and intracellular GSH-depletion of MBP

GSH levels were measured using a GSH Assay Kit. MBP nanoemulsions with the same Mn concentrations (500 μg/mL) were mixed with 10 mmol/L GSH and incubated at room temperature for different durations (0, 30 min, 1, 3, 5, 7, 8.5, and 24 h). The samples were then centrifuged for 10 min at 10,000 rpm (Thermo Biofuge Stratos, Waltham, MA, USA), and the supernatant was collected to determine the GSH level according to the manufacturer's instructions of GSH Assay Kit.

The 4T1 cells in a logarithmic growth phase were plated on a cell-culture dish and cultured at 37 °C with 5% CO_2 for 24 h. MBP were added and cultured for 0, 0.25, 0.5, 2, 4 and 6 h at a Mn concentration of 25 μg/mL. The GSH contents in the cells were measured according to the manufacturer's instructions of the GSH Assay Kit.

2.10. In vitro reactive oxygen species (ROS) detection

The level of cellular ROS in tumor cells after MBP treatment was measured by a ROS-sensitive probe, DCFH-DA. In brief, 4T1 cells were seeded in confocal dishes and cultured at 37 °C with 5% CO_2 for 24 h. Then 4T1 cells were incubated with MBP nanoemulsions at a Mn concentration of 25 μg/mL for 0, 2, 4, and 6 h or at different Mn concentrations (0, 12.5, 25, and 50 μg/mL) for 4 h. At the preset time points, 4T1 cells were treated with

DCFH-DA (20 μmol/L) for 30 min and stained with DAPI according to the manufacturer's protocols. The cells were imaged on a CLSM (Carl Zeiss, Germany).

2.11.   In vitro detection of ICD biomarkers

Calreticulin expression was detected by the calreticulin rabbit monoclonal antibody. Briefly, 4T1 cells were seeded in confocal dishes and cultured at 37 °C with 5% CO_2 for 24 h. Then 4T1 cells were incubated with MBP nanoemulsions at 25 μg/mL of Mn for 0, 2, 4, and 6 h. At the preset time points, cells were washed 3 times with PBS, fixed with 4% paraformaldehyde for 5 min and incubated with blocking solution overnight at 4 °C. Afterward, the calreticulin rabbit monoclonal antibody was added to 4T1 cells overnight at 4 °C. After wash twice with PBS, 4T1 cells were stained with Alexa Fluor 555 secondary donkey anti-rabbit IgG (H+L) in the dark for 60 min at room temperature. Cell nuclei were stained with DAPI before observation by CLSM.

To detect the ATP and HMGB1 release after MBP plus HIFU treatment, 4T1 cells were then grouped and treated as follows: control, MBP (6.25 μg/mL), HIFU (8.5 W, 1 min), and MBP H+ (6.25 μg/mL+ 8.5 W, 1 min). ATP and HMGB1 concentrations in the cell supernatant were evaluated using an ATP Assay Kit and an HMGB1 ELISA Kit, according to the manufacturer's instructions, respectively. For the ATP measurement, we used the phosphomolybdic acid colorimetric method to detect the generation of creatine phosphate. After the sample was processed according to the kit steps, the absorbance OD value was measured at 636 nm wavelength, and ATP content was calculated based on the OD value. The detection of HMGB1 was based on the enzyme-linked immunosorbent assay. After the sample was processed according to the kit steps, the 450 nm wavelength was selected to determine the absorbance OD value, and the HMGB1 content was calculated based on the OD value.

2.12.   Ex vivo optimization of HIFU parameters

To explore the relationship between the ablation volume and HIFU parameters (power and duration), the degassed excised beef livers were irradiated by HIFU at 8.5 and 10.9 W for 5, 10, 15, and 20 s, respectively. To further assess the effectiveness of enhancing HIFU irradiation by the MBP nanoemulsions, the degassed *ex vivo* mouse livers received an injection of 100 μL of MBP or MB at a Mn dose of 20 μg. Then, the injection areas of livers were irradiated by HIFU at 8.5 W for 10 s. After HIFU treatment, the treated livers were photographed and the ablation volumes in livers were measured using the following Eq. (1)[24]:

$$V = \pi \times L \times \frac{W^2}{6} \qquad (1)$$

where L is length and W is width.

2.13.   In vivo CT/MR imaging of tumors

When the average tumor volume reached around 200 mm^3, the xenograft 4T1 tumor-bearing nude mice were imaged using CT and MRI. The xenograft 4T1 tumor-bearing nude mice were conducted on a clinical 3 T MRI and Aquilion™ Prime 128 CT by intravenous injection of MBP nanoemulsions at the Mn dose of 10 mg/kg. The MRI scans and CT scans were performed at different time points after MBP injection.

2.14.   In vivo fluorescence imaging and tissue biodistribution of MBP

When the average tumor volume reached around 200 mm^3, the 4T1 tumor-bearing nude mice were intravenously injected with 100 μL of DiD-labeled MBP at a DiD dose of 3 μg and then fluorescence imaging was conducted by an IVIS Spectrum imaging system (PerkinElmer, USA) equipped with a DiD filter set (excitation/emission, 640/670 nm) at various time points (0.5, 1, 2, 4, 6, 8, 20, and 24 h). Twenty-four hours post injection, the mice were sacrificed, followed by heart perfusion with saline, and the major organs (such as heart, liver, spleen, lung and kidney) were sampled for *ex vivo* fluorescence imaging by the IVIS Spectrum imaging system (PerkinElmer, USA). The fluorescence intensity of the major organs was measured by IVIS Lumina XRMS Series III.

2.15.   Validation of tumor targeting of MBP in vivo

When the average tumor volume reached around 200 mm^3, the xenograft 4T1 tumor-bearing nude mice were intravenously injected with cou-6-labeled MBP at a cou-6 dose of 1.5 μg. Two hours later, mice were killed, and the tumors were excised for the preparation of tissue sections. Tumor tissues were fixed in 4% paraformaldehyde for 24 h. The tumor tissue sections were further incubated with the anti-SPARC antibody for 1 h at 37 °C. After washing 3 times with PBS for 3 min, the tissue sections were incubated with the second antibody for 0.5 h at 37 °C. Then, sections were stained with DAPI for 10 min at 37 °C, washed with PBS, and sealed with resin. Lastly, the sections were imaged on a CLSM (Carl Zeiss, Germany).

2.16.   In vivo antitumor efficacy and immunity of MBP treatment

The subcutaneous 4T1 xenograft tumor and lung metastatic model was prepared for evaluating the antitumor efficacy and immunity of MBP. Seven days after 4T1 inoculation, when the average tumor volume reached around 100 mm^3, tumor-bearing mice were randomly divided into four groups with eight mice in each group to receive various treatments including PBS, MBP, HIFU, HIFU plus MBP (MBP H+). The mice in PBS, MBP and MBP H+ groups were intravenously injected with PBS or MBP nanoemulsions (10 mg/kg of Mn) every other day for a total of 9 injections. One hour after the first injection, the mice in HIFU and MBP H+ groups were further irradiated by HIFU at 8.5 W for 20 s. Body weight and tumor volume of mice were monitored every 2 days. The tumor volume was calculated by the following Eq. (2)[27]:

$$V_{tumor} = L \times \frac{W^2}{2} \qquad (2)$$

where L is length and W is width.

We next sought to assess the tumor cell apoptosis induced by various treatments. Toward this objective, three mice from each group were euthanized at 72 h after the first treatment. The tumors were harvested and subjected to histological treatments, including H&E staining and TUNEL staining using the routine protocols. As for the evaluation of the anti-metastasis effect, the lung tissues from 4 groups at 3 days and 2 weeks after the first treatment were collected for H&E staining, and lung-tissue sections were assessed by a microscope to detect the metastatic lesions.

To evaluate the CALR and HMGB1 expression of tumor cells *in vivo*, tumor tissue sections were stained with anti-calreticulin antibody or anti-HMGB1 antibody and then incubated with the second antibody for 0.5 h at 37 °C. Next, tumor sections were stained with DAPI for 10 min at 37 °C, washed with PBS, and sealed with resin. Afterward, the sections were imaged on a fluorescence microscope (Leica, Germany).

As for the study of antitumor immunity in tumors, 72 h after the first treatment, tumors were harvested and digested to obtain single-cell suspension using the mouse dendritic cell isolation kit and tumor-infiltrating tissue lymphocyte separation kit, according to the manufacturer's instructions, respectively. Cell suspensions were then labeled with the mixture of FITC anti-mouse CD11c, PE anti-mouse CD86, and APC anti-mouse CD80 antibody to identify the mature DCs, or with FITC anti-mouse CD3, APC anti-mouse CD4, and PE anti-mouse CD8 antibody to identify the activated effector T cells. The immune cell proportions in cell suspensions were detected by a flow cytometry (BD, USA). At 3 and 15 days after the first treatment, part of the mice was sacrificed, and the primary organs (heart, liver, spleen, lung, and kidney) were harvested for H&E staining and microscopic examination (Leica, Germany).

2.17. In vivo biosafety of MBP

Healthy female BALB/c mice were intravenously injected with MBP at a Mn dose of 10 mg/kg. The control group was injected with PBS. After 3 and 15 days, the mice were sacrificed, and the
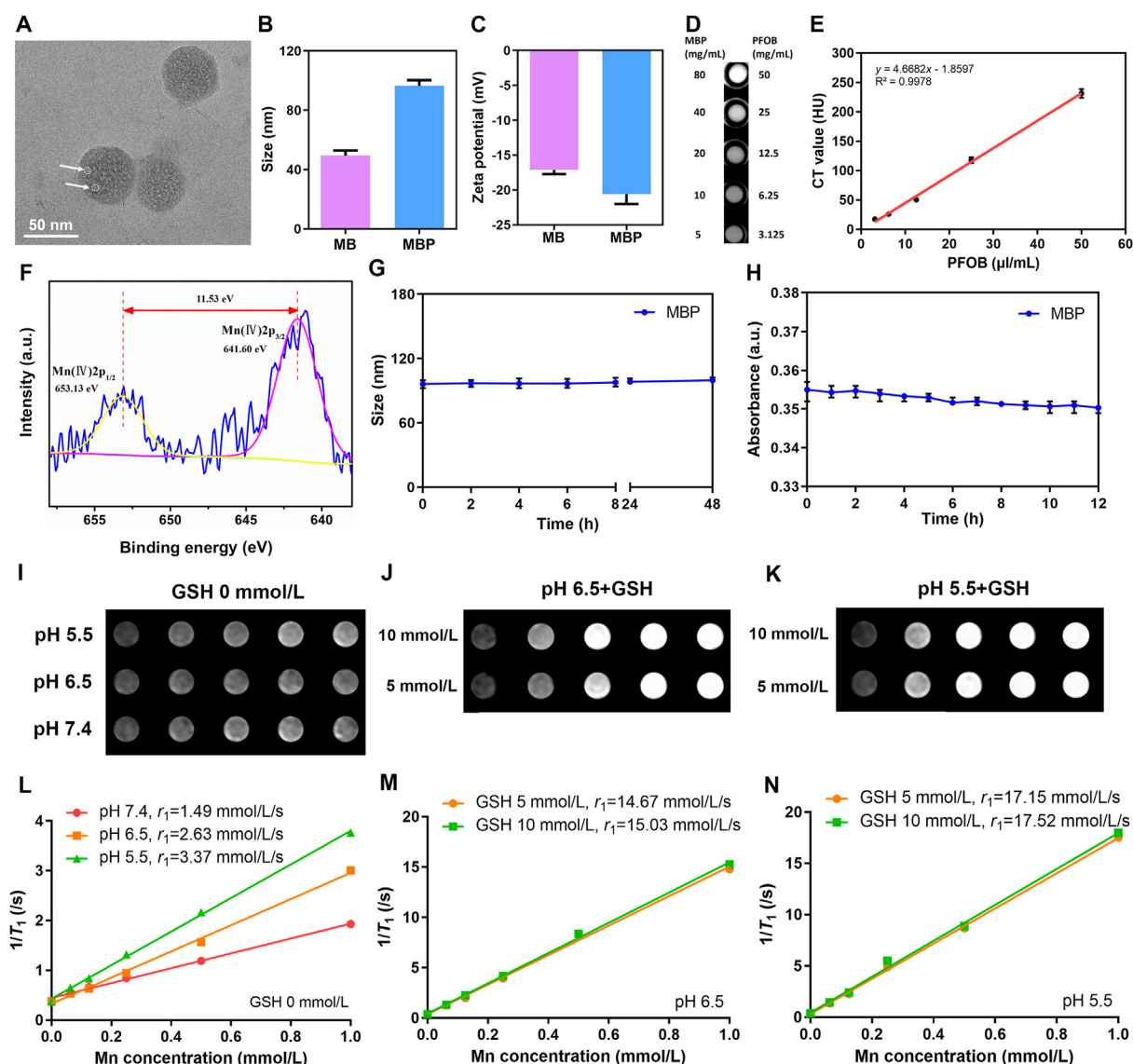

Figure 2 Characterization of MBP nanoemulsions. (A) TEM images of MBP. White arrows indicated rough surface likely caused MnO_2 nanocrystals. (B) Size and (C) zeta potential of MB and MBP ($n = 3$). (D) *In vitro* CT images of MBP nanoemulsions at different concentrations. (E) The linear curve of CT values *vs.* the PFOB concentration of MBP nanoemulsions. (F) XPS spectra of MBP. Stability of MBP (G) in PBS at 4 °C for 48 h and (H) in FBS at 37 °C for 12 h ($n = 3$). (I) *In vitro* T_1-weighted MR images of MBP treated with PBS of various pH values. (J) *In vitro* T_1-weighted MR images of MBP treated with PBS of pH 6.5 containing various concentrations of GSH. (K) *In vitro* T_1-weighted MR images of MBP treated with PBS of pH 5.5 containing various concentrations of GSH. (L)–(N) Linear curves of $\Delta 1/T_1$ *vs.* the Mn concentration of MBP nanoemulsions under different conditions ($B_0 = 3.0$ T); the slope indicated the specific relaxivity (r_1).

primary organs (heart, liver, spleen, lung, and kidney) were harvested for H&E staining and microscopic examination (Leica, Germany).

2.18. Statistical analysis

Data were expressed as mean $\pm$ standard deviation (SD). Statistical analysis and plotting of graphs were performed by GRAPHPAD Prism® and illustrated by Adobe Photoshop® software. Unpaired Student's t-test was employed for statistical analyses between two groups, and one-way ANOVA with Tukey

post-hoc analysis was used for multiple group comparison. Significance levels were determined at levels of $^*P < 0.05$, $^{**}P < 0.01$, $^{***}P < 0.001$, and $^{****}P < 0.0001$.

3. Results and discussion

3.1. Characterization of MB and MBP

In the present study, MB nanoparticles were prepared via the biomineralization method using BSA as a template. Firstly, Mn^{2+} could be facilely chelated with multiple carboxyl groups in
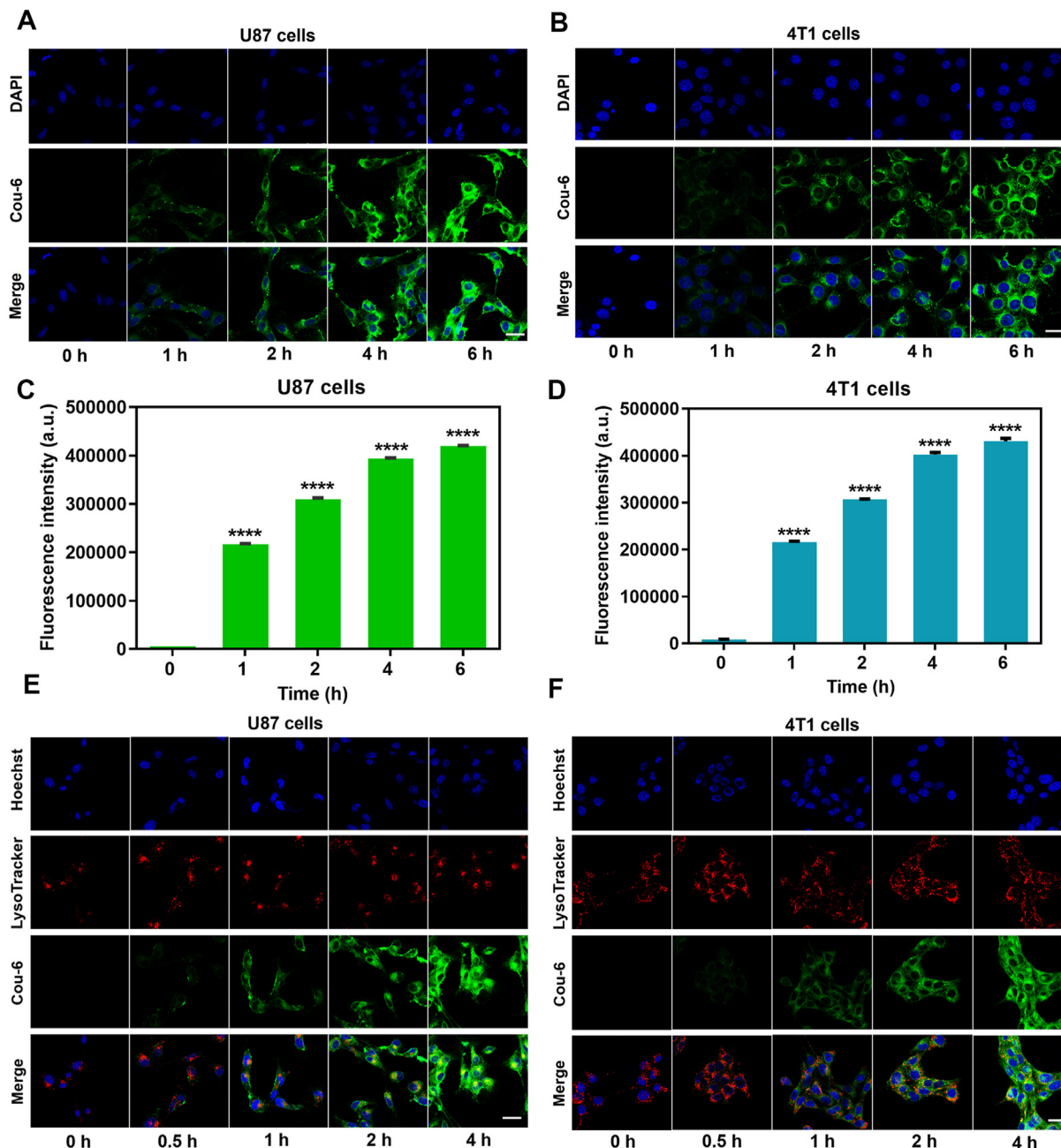

Figure 3   Cellular uptake of MBP nanoemulsions ($n = 3$). (A) Qualitative and (C) quantitative measurement of in vitro cellular uptake of Cou-6-labeled MBP nanoemulsions by U87 cells. (B) Qualitative and (D) quantitative measurement of in vitro cellular uptake of Cou-6-labeled MBP nanoemulsions by 4T1 cells. ***$P < 0.0001$ compared with 0 h. (E) and (F) Co-localization of MBP nanoemulsions with a lysosome-tracker in (E) U87 and (F) 4T1 cells. Scale bar = 25 μm.

albumin (*i.e.*, BSA)[28,32−34]. Then, BSA was stretched under the alkaline condition (pH 11−12), which consequently facilitated the formation of BSA nanoclusters with aids of Mn^{2+} coordination, yielding MnO_2 in the expansive cavity of albumin. MBP nano-emulsions were synthesized *via* ultrasonic emulsification using MB in an aqueous solution[25,29,35]. The morphology of the MBP was characterized by TEM, which revealed their spherical shape and relatively uniform size distribution (Fig. 2A). The hydrody-namic diameters of MB and MBP were approximately 49.3 ± 2.05 and 96.4 ± 2.28 nm, respectively, as determined by DLS (Fig. 2B). Furthermore, the zeta potential of MB and MBP in deionized water was −17.1 and −20.6 mV, respectively (Fig. 2C). According to the ICP-OES results, the mass ratio of manganese (Mn) was 2% in MB. The loading capability of PFOB in MBP nanoemulsions was 73.8 ± 2.1%. The XPS spectra identified the specific peaks of Mn (IV, 2p1/2) and Mn (IV, 2p3/2) at the binding energy of 653.13 and 641.60 eV (Fig. 2F), respectively, demon-strating the valence state of Mn element in nanoemulsions was IV. No significant hydrodynamic size change of MBP was noticed within 2 days (Fig. 2G) and the OD values of 580 nm for 12 h at 37 °C in FBS also showed no evident change (Fig. 2H), indicating their excellent stability.

3.2. In vitro CT and MR imaging of MBP

To assess the MRI contrast enhancement ability of MBP, the longitudinal molecular relaxivity (r_1) was evaluated in various pH values (7.4, 6.5, and 5.5) and different GSH concentrations (0, 5, and 10 mmol/L). As shown in Fig. 2I–K, MRI signal in-tensities of MBP increased with Mn concentration in various conditions. After linear fitting, a good linear correlation between T_1 relaxation (r_1) and the Mn concentration was established. As shown in Fig. 2L, the r_1 relaxivity is 1.49 mmol/L/s in neutral PBS, and only 1.76-fold and 2.26-fold increases were observed

when the pH value decreased to 6.5 and 5.5, respectively. However, the r_1 value of MBP was maximally increased to 17.52 mmol/L/s under high GSH conditions (pH 5.5 PBS), exhibiting approximately 11.8-fold higher than that in neutral PBS without GSH (Fig. 2L−N). The results demonstrated that MBP had markedly higher r_1 in high-GSH conditions than that in the normal physiological milieu, suggesting the potential of MBP as a GSH-responsive T1 MRI contrast agent for targeted tumor imaging. The higher r_1 of MBP was due to the released Mn^{2+} under high GSH conditions[36].

In order to evaluate the CT imaging ability of MBP, CT images of MBP with various PFOB concentrations were acquired. PFOB has been proven to be a great candidate for CT contrast agent[22,37]. CT images of MBP nanoemulsions with different PFOB concen-trations were presented (Fig. 2D) and Hounsfield unit (HU) values correlated linearly with PFOB concentration (Fig. 2E). Therefore, MBP possessed excellent properties for MRI/CT dual-modality biomedical imaging.

3.3. In vitro cellular uptake and co-localization of MBP with lysosomes

The cellular uptake of cou-6-labeled MBP in 4T1 and U87 cells was analyzed by confocal microscopy and flow cytometry. As shown in Fig. 3A–D and Supporting Information Fig. S1, the cellular uptake of MBP by 4T1 or U87 cells significantly increased with increasing incubation time (from 0 to 6 h) but gradually reached the equilibrium state by 4 h.

The subcellular distribution of MBP was examined by CLSM. Cou-6-labeled MBP were co-incubated with 4T1 or U87 cells for 0, 0.5, 1, 2, and 4 h. As shown in Fig. 3E–F and Supporting In-formation Figs. S2 and S3, no significant co-localization of MBP with lysosomes was observed within 0.5 h. The merged images showed co-localization fluorescence appeared orange after 1 h and
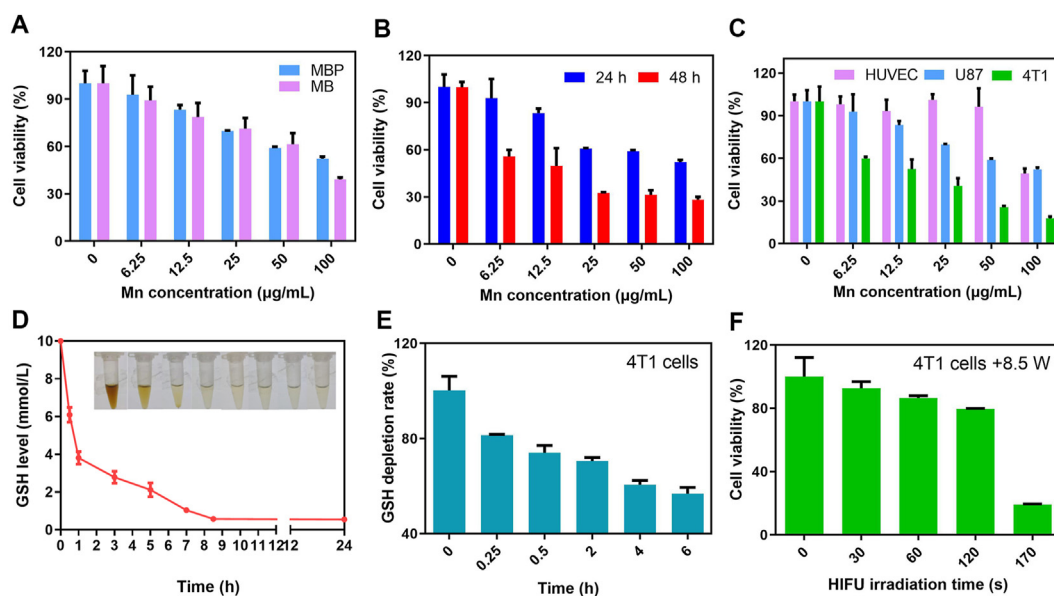

Figure 4 Cytotoxicity and GSH depletion capability of MBP nanoemulsions ($n = 3$). (A) Cytotoxicity of MBP nanoemulsions and MB nanoparticles on U87 cells after 24 h incubation. (B) Cytotoxicity of MBP nanoemulsions on U87 cells after 24 and 48 h incubation. (C) Cytotoxicity of MBP nanoemulsions against HUVEC cells, U87 cells and 4T1 cells after 24 h incubation. (D) The GSH levels of the solution after treatment with MBP nanoemulsions. (E) The GSH levels in 4T1 cells after treatment with MBP nanoemulsions. (F) Cytotoxicity of HIFU irradiation on 4T1 cells at 8.5 W for different durations.

more green fluorescence appeared in the cell cytoplasm after 2 h, which indicated that MBP could enter the cytoplasm after internalization, although the mechanism was still unknown. GSH is the main low-molecular-weight thiol in cells. About 90% of the cellular GSH is located in the cytosol, with the remainder in cellular organelles such as the mitochondria, endoplasmic reticulum, and nucleus[38,39]. Therefore, MBP could escape from lysosomes and deplete GSH in the cytoplasm.

3.4. In vitro cell viability test

To evaluate the cytotoxicity elicited by PFOB, the viability of U87 treated with MBP or MB containing the same Mn concentration was similar and there was no statistical difference in the cell viability of two groups ($P > 0.05$, Fig. 4A). The half-maximal inhibitory concentrations (IC_{50}) of MBP or MB against U87 were

17.77 and 23.69 μg/mL, respectively. This result shows that PFOB had no obvious toxicity to cells. After being incubated with MBP with different Mn concentrations for 24 and 48 h, U87 viability shows concentration and time-dependent inhibitions (Fig. 4B). MBP produced stronger cytotoxic effects on U87 cells when the incubation time was prolonged from 24 (IC_{50} 15.13 μg/mL) to 48 h (IC_{50} 4.72 μg/mL).

The viability of HUVEC, U87, and 4T1 cells treated with MBP having different Mn concentrations ranging from 0 to 100 μg/mL for 24 h is shown in Fig. 4C. The IC_{50} of MBP for HUVEC, U87, and 4T1 cells were 53.53, 17.77 and 7.80 μg/mL, respectively. Among these three kinds of cells, the cytotoxicity of MBP against 4T1 cells was the greatest, followed by U87 and HUVEC. This can be attributed to the fact that tumor cells have approximately 4-fold higher levels of GSH than that in normal cells[14−16]. Besides, GSH levels tend to be elevated in breast
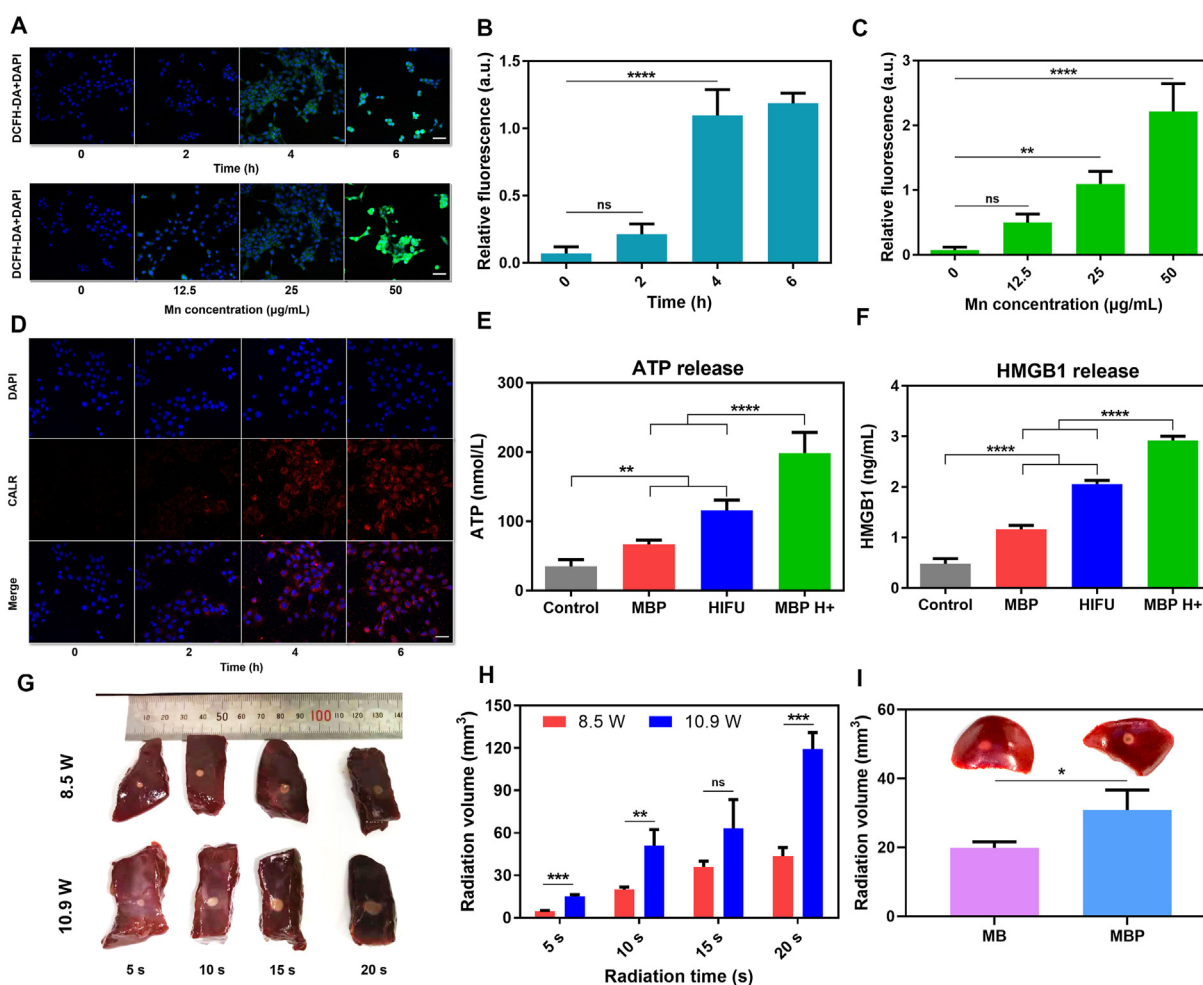

Figure 5 *In vitro* HIFU-eliciting immunogenic cancer cell death enhanced through MBP emulsions and *ex vivo* optimization parameters of HIFU irradiation ($n = 3$). (A) DCFH-DA assay demonstrated ROS generation in 4T1 cells treated with 25 μg/mL of MBP nanoemulsions for different times or different concentrations of MBP nanoemulsions (0, 12.5, 25, and 50 μg/mL) for 4 h. Scale bar = 50 μm. (B, C) ROS generation in image (A) was semi-quantified by ImageJ. (D) Immunofluorescence microscopy of CALR expression on 4T1 cell surface after MBP treatment. Scale bar = 50 μm. (E) ATP released in the culture medium after 4T1 cells were treated with MBP plus HIFU irradiation. (F) HMGB1 released in the culture medium after 4T1 cells were treated with MBP plus HIFU irradiation. (G) Digital photographs and (H) the corresponding radiation volume of beef liver samples irradiated by HIFU at 8.5 and 10.9 W for different times, respectively. (I) Digital photographs and the corresponding radiation volume of HIFU-irradiated mouse liver samples injected with MB or MBP nanoemulsions. *$P < 0.05$, **$P < 0.01$, ***$P < 0.001$, and ****$P < 0.0001$. The mark "ns" indicated no significance.
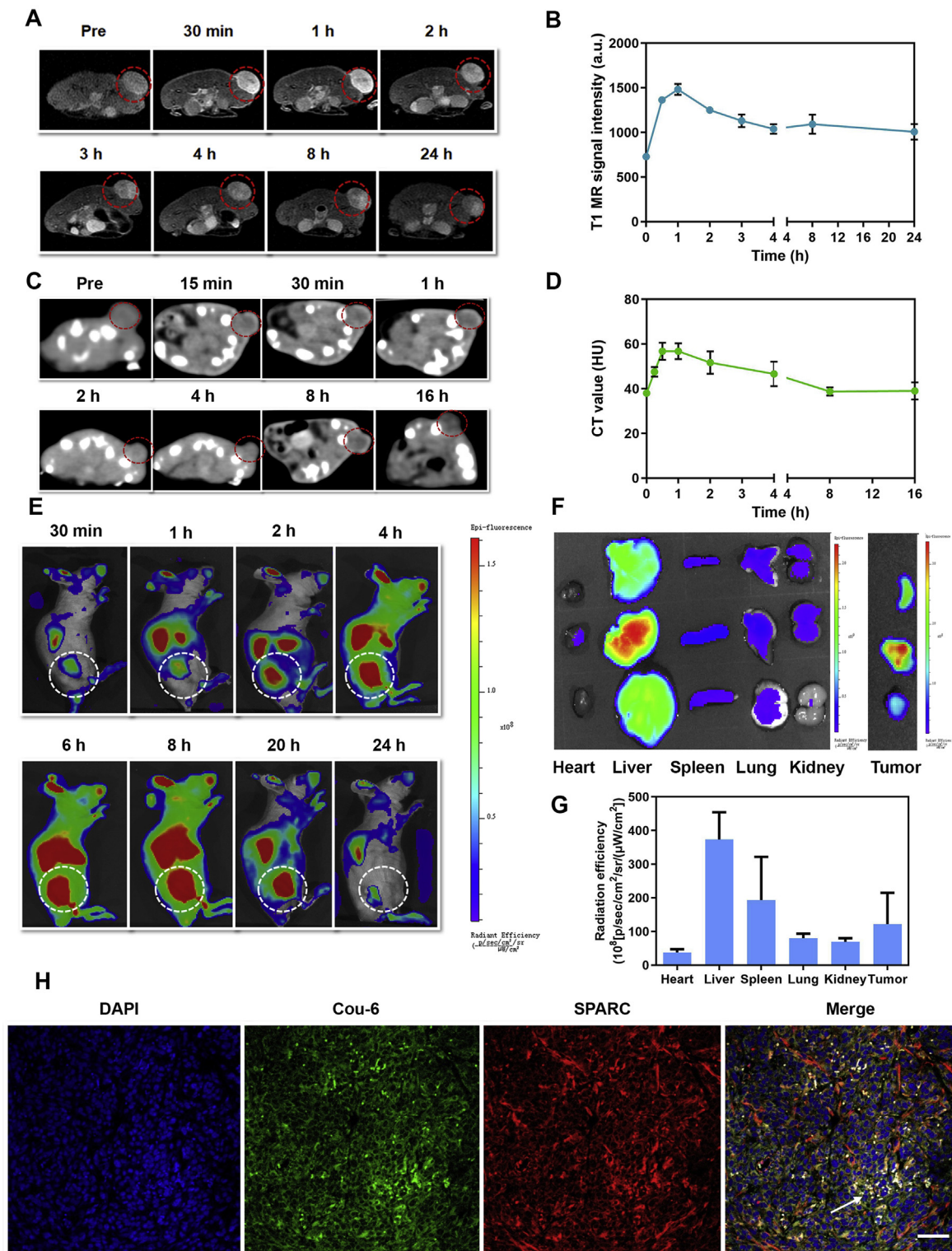
Figure 6 *In vivo* dual-modality imaging and tumor targeting behavior of MBP nanoemulsions ($n = 3$). (A) *In vivo* T_1-weighted MRI of tumor-bearing mice at different time points after the intravenous injection of MBP ($B_0 = 3.0$ T). (B) T_1-weighted MRI signal intensity changes of tumors with time following the intravenous injection of MBP. (C) *In vivo* CT imaging of tumor-bearing mice at different time points after the intravenous injection of MBP. (D) CT value changes of tumors with time following the intravenous injection of MBP. (E) *In vivo* fluorescence images of tumor-bearing mice taken at different time points after the intravenous administration of DiD-labeled MBP. (F) *Ex vivo* fluorescence images and (G) the corresponding fluorescence intensity of major organs and tumors dissected from mice bearing subcutaneous 4T1 tumors 24 h post MBP injection. (H) Immunofluorescence images of SPARC (red) expression, cou-6-labeled MBP (green) and their co-localization in tumor slices. Scale bar = 50 μm.

cancers (250−2000 nmol/g tissue), and conversely, brain tumors exhibit lower tissue levels of GSH compared with healthy tissues[40].

To further assess the effects of HIFU duration on cell viability, 4T1 cells were irradiated by HIFU at 8.5 W for different durations. After HIFU irradiation at 8.5 W for 0, 30, 60, 120, and 170 s, the temperature of cell suspensions was increased from 25 °C to around 41, 55, 69, and 82 and 98 °C, respectively, and the viability of 4T1 cells was $100.1 \pm 12.1\%$, $92.6 \pm 4.2\%$, $86.6 \pm 1.4\%$, $79.6 \pm 0.3\%$, and $19.2 \pm 0.4\%$, respectively (Fig. 4F). Therefore, HIFU irradiation at 8.5 W for no more than 60 s was adopted for cell treatment *in vitro*.

3.5. In vitro and intracellular GSH depletion of MBP

To assess *in vitro* and intracellular GSH depletion, the GSH depletion rates of MBP were calculated. *In vitro*, the GSH concentration decreased from 10 to 3.48 mmol/L in 1 h (Fig. 4D), and the mean GSH depletion velocity was calculated as 1.11 mmol/L·h. The color of the MBP was gradually lighter along with the time and GSH concentration (Supporting Information Fig. S4), indicating MBP was beneficial for GSH consumption. As shown in Fig. 3E, the GSH levels in 4T1 cells treated with MBP decreased rapidly with increasing incubation time, indicating MBP could deplete intracellular GSH effectively.

3.6. In vitro ROS detection

To assess whether ROS generation is associated with MBP concentration and duration, we employed DCFH-DA to detect the ROS production in tumor cells after MBP treatment. The ROS production significantly increased with increasing incubation time but gradually reached the equilibrium state by 4 h (Fig. 5A and B), indicating MBP might reach the maximum GSH depletion capability at 4 h after incubation with 4T1 cells. Moreover, after being incubated with MBP with different Mn concentrations for 4 h, the ROS production of 4T1 showed concentration-dependent increase (Fig. 5A and C). These results show that due to the GSH depletion by MBP, the intracellular oxidative stress was elevated[27,36,41].

3.7. In vitro detection of ICD biomarkers

We determined whether HIFU irradiation and MBP could initiate the release of DAMPs from injured and dying cells, which can induce ICD[42,43]. These DAMPs include surface exposure of CALR and the release of ATP and HMGB1. CALR is a part of the DAMPs signal, which can enhance the receptor-mediated uptake, processing, and presentation of tumor antigens to induce antitumor immunity[44]. The membrane surface-exposed CALR after MBP and HIFU treatment was analyzed by CLSM (Fig. 5D), which revealed a time-dependent exposure and was most highly expressed at 6 h. The results in Fig. 5E and F shows that MBP treatment or HIFU treatment could induce ATP and HMGB1 release from 4T1 cells while MBP H+ treatment induced a significantly higher level of ATP and HMGB1 release compared with MBP treatment or HIFU treatment. Therefore, these results indicate that HIFU irradiation plus MBP treatment could be an extremely powerful way to induce tumor ICD.

3.8. Ex vivo optimization parameters of HIFU

The ablation volume increased with the irradiation power or duration of HIFU (Fig. 5G and H). The optimized ablation volume of HIFU was well-matched with the tumor size to minimize the damage to normal tissues surrounding the tumor site. Therefore, according to HIFU ablation volume, we chose the "8.5 W for 20 s (43.5 ± 6.13 mm^3)" as the suitable condition of HIFU irradiation for the present therapy *in vivo*. In addition, as shown in Fig. 5G and I, the mean ablation volume of the mouse liver in the MBP group (30.83 ± 5.84 mm^3) was significantly greater than that in the MB group (19.89 ± 1.74 mm^3). The significantly increased ablation volume in the MBP group was mainly due to the rapid vaporization of the PFOB triggered *via* HIFU irradiation, suggesting that the encapsulated PFOB could enhance the HIFU ablation efficiency in the MBP group compared with the MB group[24,30].

3.9. In vivo CT/MR imaging

Dual-modality imaging is a hopeful technique combining the advantages of each imaging modality. In this work, multifunctional MBP could perform two combined modalities: MR and CT imaging. In order to verify the dual-modality imaging capability, MBP was intravenously injected into the 4T1 tumor-bearing nude mice. The mean T_1-weighted MRI signal intensity in the tumor area revealed a time-dependent manner. It was increased at 0.5 h after injection, reached the peak at 1 h after injection, and then gradually decreased (Fig. 6A and B). The T_1WI signal intensity at 1 h after injection was approximately 2.03 times higher than that before the injection (1482.75 ± 62.6 *vs.* 729.26 ± 23.75, $P < 0.001$). The MRI contrast enhancement could still be detected after 24 h, indicating the accumulation of MBP and the released Mn^{2+} at the tumor site. Similar to MRI, the mean CT value in the tumor area revealed a time-dependent manner. It was increased at 15 min after injection, reached the peak at 1 h after injection and then gradually decreased (Fig. 6C and D). A significant CT enhancement was found in the tumor site, with HU values increasing from 38.0 ± 1.6 HU before injection to 56.7 ± 3.5 HU at 1 h after injection. These results demonstrate that MBP could be applied as an MRI/CT dual-modality imaging contrast agent.

3.10. Tumor targeting and tissue bio-distribution of MBP

Compared with CT and MRI, fluorescence imaging has many advantages, such as no ionizing radiation, high sensitivity, high spatial resolution, noninvasive real-time imaging, and a large field of vision[45]. *In vivo* fluorescence imaging is widely used for preclinical research, such as monitoring of the therapeutic efficacy and pharmacokinetic imaging[46]. *In vivo* fluorescence imaging was performed at different time points by detecting the DiD fluorescence. As shown in Fig. 6E, the mice were found with fluorescence signals at 0.5 h post-injection. Over time, the fluorescence intensity of the tumor site increased and remained strong 20 h post-injection, illustrating effective retention of MBP at the tumor site.

To assess the distribution of MBP more precisely, the tumors and major organs were collected for *ex vivo* fluorescence imaging at 24 h post-injection. As shown in Fig. 6F and G, MBP mainly accumulated in the liver and spleen and the fluorescence intensity at the tumor region was also high. These results suggest that MBP could have a tumor-targeting effect, and the main pathway for its
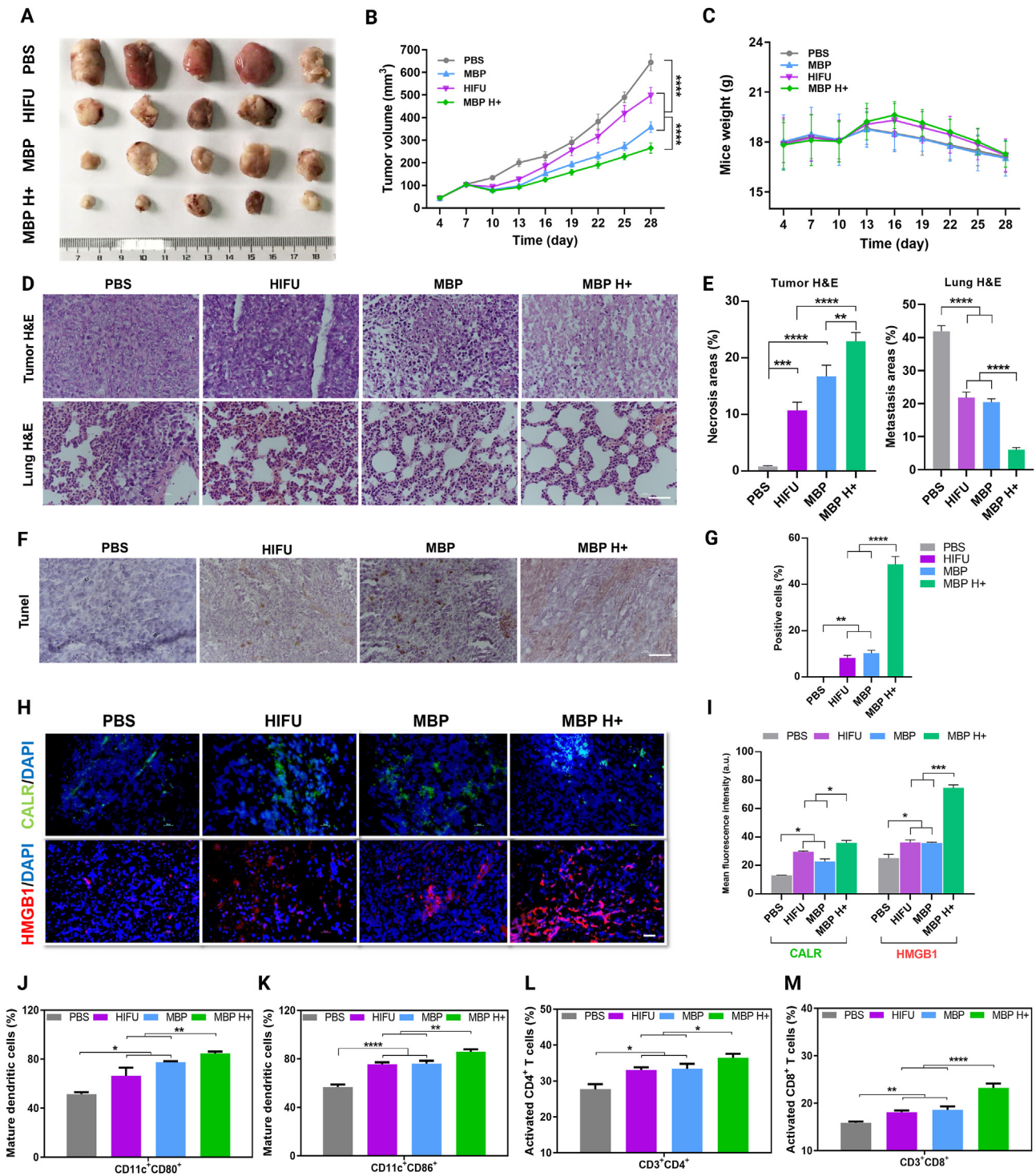
Figure 7 *In vivo* antitumor efficacy and immunity ($n = 5$). (A) Photos of tumors in four treatment groups. (B) Tumor growth curves of mouse models from four treatment groups. (C) Mouse body weight changes of four treatment groups. (D) H&E staining assay of tumor tissues and lung tissues of four treatment groups. Scale bar $= 20$ μm. (E) Necrosis area in the primary tumor and metastasis area in the lung of four treatment groups. (F) TUNEL assay of 4T1 tumor tissues of four treatment groups. Scale bar $= 20$ μm. (G) Percentages of TUNEL-positive cell in 4T1 tumor tissues of four treatment groups. (H) Immunofluorescence images of tumor sections stained with specific antibodies against CALR and HMGB1, the major delegates of DAMPs (CALR, green; HMGB1, red; Nuclei, blue). (I) Mean fluorescence intensity of the stained tumor sections in terms of the CALR and HMGB1. (J) The percentages of CD80$^+$ cells in DCs in tumors analyzed with flow cytometry at 72 h after treatment. (K) The percentages of CD80$^+$ and CD86$^+$ cells in DCs in tumors analyzed with flow cytometry at 72 h after treatment. (L) The percentages of activated CD4$^+$ T cells in tumors analyzed with flow cytometry at 72 h after treatment. (M) The percentages of activated CD8$^+$ T cells in tumors analyzed with flow cytometry at 72 h after treatment.*$P < 0.05$, **$P < 0.01$, ***$P < 0.001$, and ****$P < 0.0001$ compared with PBS or MBP H+.

metabolism be *via* the liver and spleen, which agreed with the distribution pattern of other nanoparticles *in vivo*[47].

Albumin is the most abundant protein in the plasma and a major nutrition source for tumor growth[48]. The GP60 receptor can increase the transendothelial transport of albumin[49,50]. Moreover, secreted protein acidic and rich in cysteine (SPARC) is present in the extracellular matrix of tumor tissue and the nanoparticles of albumin can actively target to tumor site *via* SPARC[51]. To validate SPARC-mediated tumor targeting of MBP, cou-6-labeled MBP were injected into 4T1 tumor-bearing nude mice. As shown in Fig. 6H and Supporting Information Fig. S5, red fluorescence, indicating the expression of SPARC proteins, was extensively observed in the cytoplasm and stroma of the tumor. The high co-localization of SPARC and MBP fluorescence signal appeared orange, indicating that the SPARC protein in the 4T1 tumor may be a target of MBP nanoemulsions.

3.11. *In vivo antitumor efficacy and immunity*

To evaluate the antitumor therapeutic efficacy of MBP plus HIFU (MBP H+) *in vivo*, 4T1 tumor-bearing mice received various treatments. The tumor growth curves showed that MBP H+ had the strongest inhibition among the four groups on the 4T1 tumor growth (Fig. 7A and B). The average tumor volume of the 4T1-bearing mice receiving HIFU, MBP, MBP H+, and PBS treatment were 498.43 ± 35.09, 357.79 ± 23.33, 265.27 ± 23.02, and 644.08 ± 36.95 mm^3, respectively. The average tumor volume of the MBP H+ treatment group was the smallest and approximately 2.5 times smaller than that of the PBS group at 21 days after the initial treatment. Therefore, MBP H+ significantly suppressed the growth of local tumors, which can be attributed to the synergistically enhanced effect of GSH depletion and HIFU ablation. To assess the side effects of MBP *in vivo*, mouse body weight changes were monitored every 2 days. No significant alteration or decrease was observed in the body weight for each group during treatment, indicating no significant side effects of these treatments (Fig. 7C).

To assess the therapeutic effects of various treatments *in vivo*, H&E and TUNEL staining were performed 72 h after the first treatment. As shown in Fig. 7D and E, tumor tissue was composed of dense tumor cells without evident necrosis in the PBS group, necrosis appeared in treatment groups and necrosis was the most evident in the MBP H+ group. Brown staining represents apoptotic cells *via* TUNEL staining (Fig. 7F). No obvious apoptotic cells were observed in the PBS group and the cell apoptosis rate was approximately 10% in HIFU and MBP groups. However, around 48 % of 4T1 tumor cells underwent apoptosis in the MBP H+ group (Fig. 7G). In brief, according to the H&E staining and the TUNEL assay, the strongest efficacy of the MBP H+ treatment can explain the tumor volume changes after treatment.

Tumor metastasis is the greatest contributor to the death of patients[52]. Thus, to evaluate whether MBP plus HIFU treatment had any effect on the distant tumors, the lung tissues from 4 groups after treatment were collected for H&E staining. It was shown that large tumor metastases were found in the PBS group, and smaller tumor metastases were found in the HIFU or MBP group. However, tumor metastasis was not observed in the MBP H+ group (Fig. 7D and E). These results suggest that MBP plus HIFU treatment not only could inhibit the local tumor but also elicit the obvious abscopal antitumor effect.

Based on *in vitro* DAMPs exposure and release of different treatments, it is necessary to verify whether MBP plus HIFU treatment could elicit ICD in tumors, by activating the innate immune system and promoting the antigen presentation to induce the abscopal antitumor effect. DAMPs such as surface-exposed CALR and passively released HMGB1 are necessary to enhance ICD of tumor cells[43,53]. As shown in Fig. 7H, PBS treatment failed to induce CALR exposure and only a little green fluorescence was observed in 4T1 tumors. Significantly stronger green fluorescence was observed in the HIFU, MBP and MBP H+ groups, compared with the PBS group, indicating the increase in CALR exposure and potent ICD effect *in vivo*. Moreover, compared with the other three groups, the MBP H+ group demonstrated a significantly higher HMGB1 signal (Fig. 7H and I). Although the detailed mechanism of HIFU-eliciting tumor ICD was not known, these results suggest MBP significantly enhanced HIFU-induced ICD effect.

DAMPs can attract receptors and ligands on DCs and activate DCs transition from immature to mature phenotype[52]. Our results show that among four treatment groups, the percentage of mature DCs (CD11c$^+$CD86$^+$ and CD11c$^+$CD80$^+$) in tumors was the highest in the MBP H+ group (Fig. 7J and K, and Supporting Information Fig. S6). The infiltration of effector T cells into tumor tissues is vital for tumor regression and the abscopal effect[27]. Next, the percentage of activated CD4$^+$ and CD8$^+$ T cells in tumors was measured, respectively. The results show the percentage of CD3$^+$CD4$^+$ and CD3$^+$CD8$^+$ T cells in MBP H+-treated tumor tissues was the highest (Fig. 7L and M, and Fig. S6), indicating that MBP plus HIFU treatment could induce the ICD-mediated antitumor immune response and consequently inhibit the growth of the primary tumor and distant metastases.

3.12. *In vivo biosafety of MBP*

The biocompatibility of MBP was further evaluated. Histological examination of the major normal organs of mice was performed to assess the potential biological toxicity at 3 and 15 days after injection with MBP nanoemulsions solution. Compared with PBS (as control), no noticeable pathological abnormality and inflammation were observed *via* the H&E stained images for both groups (Supporting Information Fig. S7). Moreover, MBP H+ treatment not only did not cause any pathological abnormality in major organs of mouse models, but also reduced the edema and inflammation of the liver, spleen and lung caused by tumor growth and metastasis (Supporting Information Figs. S8–S11).

4. Conclusions

In the present study, we successfully constructed a theranostic nanoagent, namely MBP, to advance HIFU-eliciting immunogenic cell death and MRI/CT dual-modality imaging. The designed nanoemulsions exhibited tunable structure and can quickly react with GSH to generate Mn^{2+} ions, which is promising for T_1-weighted MR imaging. Meanwhile, the MBP nanoemulsions displayed excellent MRI/CT dual-modality imaging ability, which allowed more accurate monitoring of the tumor-targeting of nanoemulsions. Furthermore, MnO$_2$ can deplete GSH, thus regulating the TME and enhancing HIFU tumor ICD. The *in vivo* experiment in both subcutaneous and metastatic models demonstrated that this hybrid nanosystem could not only suppress the

primary tumor directly but also restrain the tumor metastasis and recurrence. Considering that the main obstacles of cancer immunotherapy involve the immunosuppressive cells, MBP nanoemulsions could elevate specific antitumor T-cell responses in both primary and abscopal tumors in the 4T1 model, bringing about tumor growth inhibition. Hence, our study provided a versatile and effective immunogenic platform for promising local and metastatic tumor treatment and bioimaging.

Acknowledgments

Author contributions

Xinping Kuai, Yuefei Zhu, Zheng Yuan and Shengyu Wang designed and performed the experiments, and interpreted the data. Linlin, Xiaodan Ye, Yi-ping Lu, and Yu Luo gave methodological support and conceptual advice. Yuefei Zhu and Xinping Kuai wrote the manuscript and analyzed the data. Zhiqing Pang, Daoying Geng and Bo Yin were in charge of the project administration and supervision guidance. All authors have read and approved the final text and consent to its publication.

Conflicts of interest

The authors declare no conflicts of interest.

Appendix A.   Supporting information

Supporting data to this article can be found online at https://doi.org/10.1016/j.apsb.2021.07.025.

References

1. Kennedy LB, Salama AKS. A review of cancer immunotherapy toxicity. *CA A Cancer J Clin* 2020;**70**:86−104.
2. Hegde PS, Chen DS. Top 10 challenges in cancer immunotherapy. *Immunity* 2020;**52**:17−35.
3. Gajewski TF, Schreiber H, Fu YX. Innate and adaptive immune cells in the tumor microenvironment. *Nat Immunol* 2013;**14**:1014−22.
4. Zhu Y, Yu X, Thamphiwatana SD, Zheng Y, Pang ZJ. Nanomedicines modulating tumor immunosuppressive cells to enhance cancer immunotherapy. *Acta Pharm Sin B* 2020;**10**:2054−74.
5. Teng C, Lin C, Huang F, Xing X, Chen S, Ye L, et al. Intracellular codelivery of anti-inflammatory drug and anti-miR 155 to treat inflammatory disease. *Acta Pharm Sin B* 2020;**10**:1521−33.
6. Galluzzi L, Buqué A, Kepp O, Zitvogel L, Kroemer G. Immunogenic cell death in cancer and infectious disease. *Nat Rev Immunol* 2017;**17**:97−111.
7. Du X, Hou Y, Huang J, Pang Y, Ruan C, Wu W, et al. Cytosolic delivery of the immunological adjuvant Poly I:C and cytotoxic drug crystals *via* a carrier-free strategy significantly amplifies immune response. *Acta Pharm Sin B* 2021;**11**:3272−85.
8. Li MO, Rudensky AY. T cell receptor signalling in the control of regulatory T cell differentiation and function. *Nat Rev Immunol* 2016;**16**:220−33.
9. Kennedy JE. High-intensity focused ultrasound in the treatment of solid tumours. *Nat Rev Cancer* 2005;**5**:321−7.
10. van den Bijgaart RJ, Eikelenboom DC, Hoogenboom M, Fütterer JJ, den Brok MH, Adema GJ. Thermal and mechanical high-intensity focused ultrasound: perspectives on tumor ablation, immune effects and combination strategies. *Cancer Immunol Immunother* 2017;**66**:247−58.
11. Kim G, Lau VM, Halmes AJ, Oelze ML, Moore JS, Li KC. High-intensity focused ultrasound-induced mechanochemical transduction in synthetic elastomers. *Proc Natl Acad Sci USA* 2019;**116**:10214−22.
12. Cohen-Inbar O, Xu Z, Sheehan JP. Focused ultrasound-aided immunomodulation in glioblastoma multiforme: a therapeutic concept. *J Ther Ultrasound* 2016;**4**:1−9.
13. Yan N, Lin L, Xu C, Tian H, Chen X. A GSH-gated DNA nanodevice for tumor-specific signal amplification of microRNA and MR imaging-guided theranostics. *Small* 2019;**15**:e1903016.
14. Lee MH, Yang Z, Lim CW, Lee YH, Dongbang S, Kang C, Kim JS. Disulfide-cleavage-triggered chemosensors and their biological applications. *Chem Rev* 2013;**113**:5071−109.
15. Kumar R, Shin WS, Sunwoo K, Kim WY, Koo S, Bhuniya S, Kim JS. Small conjugate-based theranostic agents: an encouraging approach for cancer therapy. *Chem Soc Rev* 2015;**44**:6670−83.
16. Fan H, Yan G, Zhao Z, Hu X, Zhang W, Liu H, Fu X, Fu T, Zhang XB, Tan W. A smart photosensitizer-manganese dioxide nanosystem for enhanced photodynamic therapy by reducing glutathione levels in cancer cells. *Angew Chem Int Ed Engl* 2016;**55**:5477−82.
17. Diehn M, Cho RW, Lobo NA, Kalisky T, Dorie MJ, Kulp AN, et al. Association of reactive oxygen species levels and radioresistance in cancer stem cells. *Nature* 2009;**458**:780−3.
18. Bi H, Dai Y, Yang P, Xu J, Yang D, Gai S, et al. Glutathione mediated size-tunable UCNPs-Pt(IV)-ZnFe$_2$O$_4$ nanocomposite for multiple bioimaging guided synergetic therapy. *Small* 2018;**14**:e1703809.
19. Lin LS, Song J, Song L, Ke K, Liu Y, Zhou Z, et al. Simultaneous Fenton-like ion delivery and glutathione depletion by MnO$_2$-based nanoagent to enhance chemodynamic therapy. *Angew Chem Int Ed Engl* 2018;**57**:4902−6.
20. Cai X, Zhu Q, Zeng Y, Zeng Q, Chen X, Zhan Y. Manganese oxide nanoparticles as MRI contrast agents in tumor multimodal imaging and therapy. *Int J Nanomed* 2019;**14**:8321−44.
21. Liang X, Fang L, Li X, Zhang X, Wang F. Activatable near infrared dye conjugated hyaluronic acid based nanoparticles as a targeted theranostic agent for enhanced fluorescence/CT/photoacoustic imaging guided photothermal therapy. *Biomaterials* 2017;**132**:72−84.
22. Zhang L, Wang D, Yang K, Sheng D, Tan B, Wang Z, et al. Mitochondria-targeted artificial "nano-RBCs" for amplified synergistic cancer phototherapy by a single NIR irradiation. *Adv Sci* 2018;**5**:1800049.
23. Ma M, Xu H, Chen H, Jia X, Zhang K, Wang Q, et al. A drug-perfluorocarbon nanoemulsion with an ultrathin silica coating for the synergistic effect of chemotherapy and ablation by high-intensity focused ultrasound. *Adv Mater* 2014;**26**:7378−85.
24. Chang N, Lu S, Qin D, Xu T, Han M, Wang S, et al. Efficient and controllable thermal ablation induced by short-pulsed HIFU sequence assisted with perfluorohexane nanodroplets. *Ultrason Sonochem* 2018;**45**:57−64.
25. Li X, Sui Z, Li X, Xu W, Guo Q, Sun J, et al. Perfluorooctylbromide nanoparticles for ultrasound imaging and drug delivery. *Int J Nanomed* 2018;**13**:3053−67.
26. Liang R, Liu L, He H, Chen Z, Han Z, Luo Z, et al. Oxygen-boosted immunogenic photodynamic therapy with gold nanocages@manganese dioxide to inhibit tumor growth and metastases. *Biomaterials* 2018;**177**:149−60.
27. Wang F, Wen L, Liu J, Peng W, Meng Z, Chen Q, et al. Albumin nanocomposites with MnO$_2$/Gd$_2$O$_3$ motifs for precise MR imaging of

acute myocardial infarction in rabbit models. *Biomaterials* 2020;**230**: 119614.

28. Wrobeln A, Laudien J, Groß-Heitfeld C, Linders J, Mayer C, Wilde B, et al. Albumin-derived perfluorocarbon-based artificial oxygen carriers: a physico-chemical characterization and first *in vivo* evaluation of biocompatibility. *Eur J Pharm Biopharm* 2017;**115**: 52−64.

29. Yu J, Yang W, Xing S, Wang J, Han H, Zhang P, et al. Blended gold/MnO$_2$@BSA nanoparticles for fluorometric and magnetic resonance determination of ascorbic acid. *Mikrochim Acta* 2019;**186**:89.

30. Yang Z, Luo S, Zeng Y, Shi C, Li R. Albumin-mediated biomineralization of shape-controllable and biocompatible ceria nanomaterials. *ACS Appl Mater Interfaces* 2017;**9**:6839−48.

31. Chen J, Chen Q, Liang C, Yang Z, Zhang L, Yi X, et al. Albumin-templated biomineralizing growth of composite nanoparticles as smart nano-theranostics for enhanced radiotherapy of tumors. *Nanoscale* 2017;**9**:14826−35.

32. Qiao Y, Zong Y, Yin H, Chang N, Li Z, Wan M. Spatial and temporal observation of phase-shift nano-emulsions assisted cavitation and ablation during focused ultrasound exposure. *Ultrason Sonochem* 2014;**21**:1745−51.

33. Wang S, Li F, Qiao R, Hu X, Liao H, Chen L, et al. Arginine-rich manganese silicate nanobubbles as a ferroptosis-inducing agent for tumor-targeted theranostics. *ACS Nano* 2018;**12**:12380−92.

34. Barnett BP, Ruiz-Cabello J, Hota P, Liddell R, Walczak P, Howland V, et al. Fluorocapsules for improved function, immunoprotection, and visualization of cellular therapeutics with MR, US, and CT imaging. *Radiology* 2011;**258**:182−91.

35. Scirè A, Cianfruglia L, Minnelli C, Bartolini D, Torquato P, Principato G, Galli F, Armeni T. Glutathione compartmentalization and its role in glutathionylation and other regulatory processes of cellular pathways. *Biofactors* 2019;**45**:152−68.

36. Wu G, Fang YZ, Yang S, Lupton JR, Turner ND. Glutathione metabolism and its implications for health. *J Nutr* 2004;**134**:489−92.

37. Gamcsik MP, Kasibhatla MS, Teeter SD, Colvin OM. Glutathione levels in human tumors. *Biomarkers* 2012;**17**:671−91.

38. Kou L, Sun R, Xiao S, Zheng Y, Chen Z, Cai A, Zheng H, et al. Ambidextrous approach to disrupt redox balance in tumor cells with increased ROS production and decreased GSH synthesis for cancer therapy. *ACS Appl Mater Interfaces* 2019;**11**:26722−30.

39. Ma Y, Zhang Y, Li X, Zhao Y, Li M, Jiang W, et al. Near-infrared II phototherapy induces deep tissue immunogenic cell death and potentiates cancer immunotherapy. *ACS Nano* 2019;**13**:11967−80.

40. Krysko DV, Garg AD, Kaczmarek A, Krysko O, Agostinis P, Vandenabeele P. Immunogenic cell death and DAMPs in cancer therapy. *Nat Rev Cancer* 2012;**12**:860−75.

41. Garg AD, Martin S, Golab J, Agostinis P. Danger signalling during cancer cell death: origins, plasticity and regulation. *Cell Death Differ* 2014;**21**:26−38.

42. Luo Z, Jin K, Pang Q, Shen S, Yan Z, Jiang T, et al. On-demand drug release from dual-targeting small nanoparticles triggered by high-intensity focused ultrasound enhanced glioblastoma-targeting therapy. *ACS Appl Mater Interfaces* 2017;**9**:31612−25.

43. Arranz A, Ripoll J. Advances in optical imaging for pharmacological studies. *Front Pharmacol* 2015;**11**:189.

44. Etrych T, Lucas H, Janoušková O, Chytil P, Mueller T, Mäder K. Fluorescence optical imaging in anticancer drug delivery. *J Control Release* 2016;**226**:168−81.

45. Lindén M. Biodistribution and excretion of intravenously injected mesoporous silica nanoparticles: implications for drug delivery efficiency and safety. *Enzymes* 2018;**43**:155−80.

46. Kratz F. Albumin as a drug carrier: design of prodrugs, drug conjugates and nanoparticles. *J Control Release* 2008;**132**:171−83.

47. Chen C, Hu H, Qiao M, Zhao X, Wang Y, Chen K, et al. Anti-tumor activity of paclitaxel through dual-targeting lipoprotein-mimicking nanocarrier. *J Drug Target* 2015;**23**:311−22.

48. Elzoghby AO, Samy WM, Elgindy NA. Albumin-based nanoparticles as potential controlled release drug delivery systems. *J Control Release* 2012;**157**:168−82.

49. Park K. Albumin: a versatile carrier for drug delivery. *J Control Release* 2012;**157**:3.

50. Zhou J, Wang G, Chen Y, Wang H, Hua Y, Cai Z. Immunogenic cell death in cancer therapy: present and emerging inducers. *J Cell Mol Med* 2019;**23**:4854−65.

51. Steeg PS. Targeting metastasis. *Nat Rev Cancer* 2016;**16**:201−18.

52. Kroemer G, Galluzzi L, Kepp O, Zitvogel L. Immunogenic cell death in cancer therapy. *Annu Rev Immunol* 2013;**31**:51−72.

53. Zhang W, Wang F, Hu C, Zhou Y, Gao H, Hu J. The progress and perspective of nanoparticle-enabled tumor metastasis treatment. *Acta Pharm Sin B* 2020;**10**:2037−53.